J. Fluid Mech. (2001), vol. 436, pp. 41–57. Printed in the United Kingdom

Aerodynamic lift and drag fluctuations of a sphere

By M. S. HOWE[1], G. C. LAUCHLE[2] AND J. WANG[2]

[1]Boston University, College of Engineering, 110 Cummington Street, Boston, MA 02215, USA

[2]Penn State University, Graduate Program in Acoustics and Applied Research Laboratory, PO Box 30, State College, PA 16804, USA

(Received 21 June 1999 and in revised form 1 December 2000)

An experimental and theoretical investigation is made of the unsteady lift and drag exerted on a sphere in a nominally steady, high Reynolds number, incompressible flow. The net force on the sphere has previously been ascribed to fluctuations in the bound vorticity in the meridian plane normal to the force, produced by large-scale coherent structures shed into the wake. A simplified model of vortex shedding is proposed that involves coherent eddies in the form of a succession of randomly orientated vortex rings, interconnected by pairs of oppositely rotating line vortices, and shed at quasi-regular intervals with a Strouhal number ~ 0.19. The rings are rapidly dissipated by turbulence diffusion, but it is shown that only the nascent vortex ring makes a significant contribution to the surface force, and that the force spectrum at Strouhal numbers exceeding unity is effectively independent of the shape of the fully formed vortex. Predictions of the lift and drag spectra at these frequencies are found to be in good accord with new towing tank measurements presented in this paper.

1. Introduction

A sphere in a nominally steady and incompressible high Reynolds number flow is subject to unsteady drag and side forces. Rayleigh (1877) attributed the side force on a spinning tennis ball to the *Magnus effect*, associated with the establishment of mean circulation about the sphere in a meridian plane at right angles to the force. For a non-spinning sphere Willmarth & Enlow (1969), Achenbach (1974), and Taneda (1978) have suggested that the circulation is caused by the asymmetric shedding of large turbulent eddies into the wake, which produces an unsteady *bound vorticity* vector (directed through the centre of the sphere) whose cross-product with the mean stream velocity determines the fluctuating force. The side component of the force has no preferred orientation in a plane normal to the free stream direction, but nonetheless it is usually referred to as the unsteady *lift*. It is responsible, for example, for the erratic path of a rising weather balloon (Scoggins 1967), and for the unpredictable trajectory of a baseball thrown at medium speed with very little spin (a 'knuckle ball') or of a cricket ball whose seam is at zero angle of incidence to its direction of motion (Barton 1982). Unsteady side and drag forces can also cause harmful vibrations in support structures (Parkinson 1989; Williamson & Govardhan 1997). Similarly, the wake-induced forces produce unsteady buffeting of spherical hydrophones moored in a water basin where a mean flow may be generated by surface waves, tidal changes, or gravity. According to Finger, Abbagnaro & Bauer (1979), Keller (1977), McEachern & Lauchle (1995) and Gabrielson, Gardner & Garrett (1995) the problem can be severe for a neutrally buoyant 'acoustic velocity' hydrophone that is designed to follow the fluid motion produced by an incident sound wave (Leslie, Kendall & Jones 1956).

Vortex shedding from a sphere at large Reynolds numbers occurs predominantly at a Strouhal number $fD/U \approx 0.2$, where f denotes frequency, D is the diameter of the sphere, and U is the undisturbed stream velocity (Achenbach 1972, 1974; Sakamoto & Haniu 1990; Taneda 1956, 1978; Willmarth & Enlow 1969; Kim & Durbin 1988; Chomaz, Bonneton & Hopfinger 1993). In addition, a higher frequency motion at a Strouhal number that increases with the Reynolds number $Re = UD/\nu$ (ν = kinematic viscosity) has been detected in measurements of the velocity fluctuations immediately behind the sphere when $Re > 800$. However, the spectrum of the unsteady lift generally turns out to be very broadband, with no significant 'discrete' contributions at either of these Strouhal numbers. Willmarth & Enlow (1969) report measurements of the lift for a sphere in air, whose spectrum exhibits smoothly varying behaviour at Strouhal numbers $\leqslant 0.3$ in the 'supercritical' range $4.84 \times 10^5 \leqslant Re \leqslant 1.67 \times 10^6$.

There have hitherto been no published measurements of the spectrum of the unsteady drag experienced by a sphere, nor of its magnitude relative to the lift. Tomboulides, Orszag & Karniadakis (1993) calculated the fluctuating drag using a 'large-eddy simulation' of the wake at $Re = 20\,000$, but made no comparison with the lift. Numerical simulations at $Re < 1000$ have also been performed by Johnson & Patel (1999), Mittal (1999) and Tomboulides & Orszag (2000); these calculations confirm that the wake becomes asymmetric when Re exceeds 350–450, and that the drag at these Reynolds numbers is five or six times larger than the lift. However, according to a numerical study by Zierke (1997), the time-dependent drag experienced by a freely falling sphere at a $Re = 1000$ is an order of magnitude *smaller* than the lift. Data presented later in this paper (§ 4) indicate that this is also true at higher Reynolds numbers, at least for Re as large as about 17 000. This is consistent with the corresponding results for a cylinder in a cross-flow (Goldstein 1965; Phillips 1956) where the root-mean-square lift is also an order of magnitude larger than that of the drag (West & Apelt 1993).

The unsteady lift and drag on a sphere in high Reynolds number flow are studied analytically in this paper in terms of a model of asymmetric vortex shedding. The investigation is motivated by the observation by Willmarth & Enlow (1969) that the large measured fluctuating forces are strongly correlated with fluctuations in the bound vorticity, which in turn is attributed to the shedding of large-scale coherent structures, even at supercritical Reynolds numbers ($Re > 3.7 \times 10^5$) when the boundary layer on the sphere is turbulent. The general characteristics of the wake have been summarized by Sakamoto & Haniu (1990) for subcritical, low and intermediate Reynolds number. In particular, 'hairpin' vortices are found in the wake when $300 < Re < 420$. When Re exceeds about 800 large-scale vortex loops are observed to move away from the sphere, rotating at random about an axis parallel to the flow through the centre of the sphere. The wake becomes turbulent at $Re \sim 2000$. At higher subcritical Reynolds numbers ($6000 < Re < 370\,000$) the separated flow becomes completely turbulent, but the velocity spectrum in the wake loses some of the broadband nature observed at lower Reynolds numbers; the Strouhal frequency of 'coherent' shedding increases with Reynolds number and then approaches the constant value of about 0.19 at $Re \sim 20\,000$.

Flow visualizations by Taneda (1978) at $Re = 3.5 \times 10^5$ reveal that the laminar

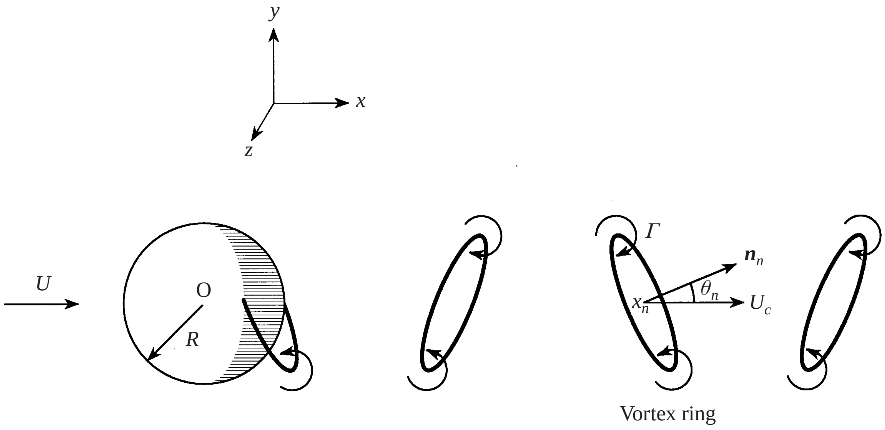

FIGURE 1. Vortex shedding from a sphere modelled by a sequence of randomly orientated vortex rings.

boundary layer on the sphere separates at $\phi \sim 100°$, where ϕ is measured from the forward stagnation point. Reattachment occurs as a turbulent boundary layer near $\phi \sim 117°$, and the turbulent layer finally separates from the sphere at about 135°. Reversed flow exists close to the surface within the separation bubble and a vortex ring is formed. The large-scale structure of the wake is similar to that observed at lower subcritical Reynolds numbers; it is asymmetric and contains a succession of hairpin-type vortices which, in the region immediately downstream of separation, appear as quasi-periodically spaced vortex loops or rings. According to Taneda, the lines of laminar and turbulent separation actually vary randomly from the nominal values quoted above by about $\pm 10°$ and $\pm 12°$ respectively. The near wake may therefore be imagined to consist of a succession of vortex rings that are connected one to another by pairs of oppositely rotating line vortices offset from the streamwise axis through the centre of the sphere; the rings are shed quasi-periodically at a Strouhal number ~ 0.19 with randomly varying orientation. These structures are rapidly dissipated at the higher Reynolds numbers by turbulence in the downstream wake but, because of their coherence during shedding, are responsible for the large-scale fluctuations in bound vorticity and for the observed lift and drag fluctuations.

On the basis of these observations, the influence of the coherent vortex structures in the near wake will be modelled by considering an ensemble of realizations of a succession of randomly orientated vortex rings, as indicated in figure 1. A crude model of this kind is evidently a gross oversimplification, if only because the vortex street would in practice be rapidly destroyed by turbulence diffusion. However, significant fluctuations in the bound vorticity can occur only during the shedding of a vortex ring, and it will be shown that the principal contribution to the surface force is indeed supplied by the nascent vortex ring, and therefore that the subsequent evolution of the vortex street has little bearing on the dominant lift and drag fluctuations experienced by the sphere. The model would need to be refined if it is also desired to incorporate modifications of the flow that occur when the sphere is located in a mean turbulent stream (Hunt *et al.* 1990), and also in applications where the influence of a neighbouring sidewall (of a wind tunnel, say) is important.

The predictions of the lift and drag spectra supplied by the model are found to be in good accord with measurements in the Strouhal number range $1 < fD/U \leqslant 40$ made by towing a sphere at constant velocity in water (Wang 1999). These Strouhal numbers are important in applications involving spherical hydrophones, and both the theoretical predictions and measurements indicate that the lift and drag spectra decrease like $1/f^3$ in this interval. This high-frequency behaviour is shown to be governed by the initial stages of vortex ring formation, and to be relatively insensitive to the geometry of the fully formed vortex ring. Predictions at lower frequencies ($fD/U < 1$) are more critically dependent on the assumed statistics of the vortex rings, and to the presence of neighbouring structures such as a wind tunnel wall, but are nonetheless consistent with the early measurements of the lift spectrum made by Willmarth & Enlow (1969).

The analytical model is formulated in § 2; formulae for the lift and drag spectra are derived in § 3. The towing tank experiment is described in § 4, where Wang's (1999) measurements are compared with predictions of the model.

2. Vortex shedding at high Reynolds number

2.1. *Vortex ring model of shed vortices*

Consider a rigid sphere of radius R situated with its centre at the origin of the rectangular coordinates (x, y, z) in the presence of a nominally steady, incompressible flow at speed U in the positive x-direction. The Reynolds number is sufficiently large that the wake flow is turbulent. The dominant characteristics of the large-scale coherent behaviour of the wake will be modelled by the sequence of vortex rings depicted schematically in figure 1. The rings are shed from the sphere quasi-periodically at frequency $\sim f_o$ and Strouhal number $f_o D/U \sim 0.2$, where $D = 2R$.

The vortex rings are assumed to translate in the mean stream direction with their centres on the x-axis at a constant convection velocity $U_c \approx 0.7U$. The nth ring has circulation Γ (in the sense illustrated in figure 1), radius a and the normal $\boldsymbol{n}_n$ to the plane of the ring makes an angle $\theta_n\,(0 \leqslant \theta_n \leqslant \pi/2)$ with the positive x-axis; the azimuthal angle between the y-direction and the plane defined by the x-axis and the normal is denoted by φ_n. Variations in the shape of a ring during shedding from the sphere are ignored. According to this view, the most important influences determining the unsteady forces on the sphere during shedding are the orientation of the rings and their mean convection velocity. Shedding is pictured to occur by the translation of each ring through the surface of the sphere, so that the duration of shedding for the nth ring is $\delta t_n = 2a \sin\theta_n/U_c$. If shedding starts for this ring at time $t = t_n$, it is complete when $t = t_n + \delta t_n$, and the position $x = x_n(t)$ of the centre of the ring on the x-axis is given by

$$x_n = U_c(t - t_n) + \sqrt{R^2 - a^2\cos^2\theta_n} - a\sin\theta_n, \quad t > t_n. \tag{2.1}$$

Figure 1 illustrates the situation when about one half of the nascent vortex ring is formed; the semi-circular arc of the ring already shed into the flow has a net circulation in the anti-clockwise sense. There will accordingly be a clockwise circulation around the sphere, producing an overall 'lift' force in the y-direction. The net circulation around the sphere decreases as more of the vortex is shed, and vanishes when the vortex separates and moves away into the wake. In this latter phase there is no mean circulation around the sphere, so that any surface forces will tend to be small until a new vortex begins to form. The proposed shedding mechanism can therefore produce quasi-periodic and potentially large-amplitude fluctuations in the lift.

2.2. *Calculation of the surface forces*

The net force exerted on the sphere in the i-direction in incompressible flow can be expressed in the form (Howe 1989, 1998)

$$F_i(t) = \rho_o \int \nabla X_i \cdot \boldsymbol{\omega} \wedge \boldsymbol{v} \, \mathrm{d}^3\boldsymbol{x} - \eta \oint_S \boldsymbol{\omega} \wedge \nabla X_i \cdot \mathrm{d}\boldsymbol{S}, \tag{2.2}$$

where ρ_o, η are respectively the mean density and shear viscosity of the fluid, $\boldsymbol{v}(\boldsymbol{x}, t)$ is the fluid velocity, and $\boldsymbol{\omega} \equiv \text{curl } \boldsymbol{v}$ is the vorticity. The integrations are taken respectively over the volume occupied by the fluid and over the surface of the sphere (where the vector surface element $\mathrm{d}\boldsymbol{S}$ is directed into the fluid), and

$$X_i = x_i \left(1 + \frac{R^3}{2|\boldsymbol{x}|^3}\right) \tag{2.3}$$

is an auxiliary function that coincides with the velocity potential of an ideal flow past the sphere that has unit speed in the i-direction at large distances from the sphere. The surface integral in (2.2) represents the surface force produced by the viscous skin friction and will be discarded, since its relative contribution at high Reynolds numbers is small. Equation (2.2) is exact for incompressible flow when the body is at rest, and its utility depends on the accuracy with which the vorticity $\boldsymbol{\omega}$ and the velocity $\boldsymbol{v}$ can be specified.

Thus, if $F_{in}(t)$ denotes the component of the force attributable to the nth vortex ring,

$$F_i(t) = \sum_{n=-\infty}^{\infty} F_{in}(t), \tag{2.4}$$

where

$$\begin{aligned} F_{in}(t) &= 0, \quad t < t_n \\ &= \rho_o \int \nabla X_i \cdot \boldsymbol{\omega}_n \wedge \boldsymbol{v} \, \mathrm{d}^3\boldsymbol{x}, \quad t > t_n, \end{aligned} \tag{2.5}$$

and $\boldsymbol{\omega}_n(\boldsymbol{x}, t)$ is the vorticity distribution of the nth vortex.

To evaluate the volume integral the cross-section of the vortex ring core is assumed to be infinitesimal. To fix ideas, consider the case in which the nth ring is orientated with its normal $\boldsymbol{n}_n$ in the (x, y)-plane (i.e. $\varphi_n = 0$). Let $s = a\xi$ denote curvilinear distance along the axis of the core in the right-handed sense with respect to $\boldsymbol{n}_n$, where the angle ξ is measured from the 'lower' point of intersection of the ring and the (x, y)-plane (where $y < 0$, see figure 2). The instantaneous velocity $\boldsymbol{v}$ must satisfy the no-slip boundary condition on the sphere, but we take $\boldsymbol{v} = (U_c, 0, 0)$ on the ring to account for uniform convection of the vortex parallel to the mean stream at constant speed U_c in the x-direction, so that

$$\boldsymbol{\omega}_n \wedge \boldsymbol{v} \, \mathrm{d}^3\boldsymbol{x} = \Gamma \, U_c(0, \cos\xi, \cos\theta_n \sin\xi) a \mathrm{d}\xi, \tag{2.6}$$

and

$$F_{in}(t) = \rho_o U_c \Gamma a \int_{-\xi_n(t)}^{\xi_n(t)} \left(\cos\xi \frac{\partial X_i}{\partial y} + \cos\theta_n \sin\xi \frac{\partial X_i}{\partial z}\right) \mathrm{d}\xi, \quad t > t_n. \tag{2.7}$$

In this formula $\xi_n(t) = \pi$ for $t > t_n + \delta t_n$, after the vortex is released by the sphere. At earlier times $\xi_n(t)$ is the angle illustrated in figure 2, determined by the points of

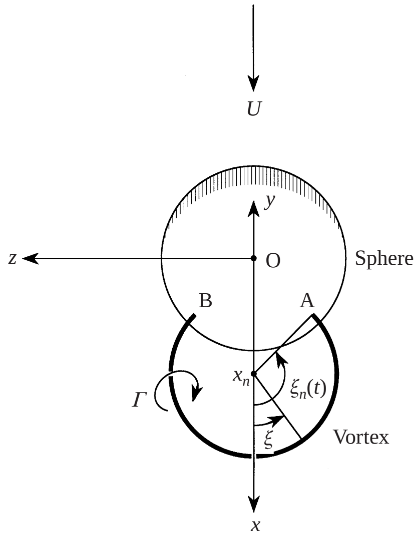

FIGURE 2. View from downstream and above of a vortex ring separating from the sphere at A and B when $\varphi_n = 0$. The angle $\xi_n(t)$ determines the total arc length $2a\xi_n(t)$ of the shed vortex during separation.

intersection (A and B in the figure) of the vortex with the surface of the sphere:

$$\xi_n(t) = \frac{\pi}{2} + \sin^{-1}\left(\frac{x_n^2(t) + a^2 - R^2}{2ax_n(t)\sin\theta_n}\right), \quad t_n < t < t_n + \delta t_n, \tag{2.8}$$

where $x_n(t)$ is the x-coordinate of the centre of the vortex ring given by (2.1). The derivatives $\partial X_i/\partial y$, $\partial X_i/\partial z$ are evaluated on the vortex ring at the integration point given parametrically by

$$\boldsymbol{x} = (x_n(t) + a\sin\theta_n\cos\xi,\ -a\cos\theta_n\cos\xi,\ -a\sin\xi). \tag{2.9}$$

2.3. *The unsteady lift and drag*

When $\varphi_n = 0$, it is evident by symmetry that the contribution $\boldsymbol{F}_n$ of the nth vortex ring to the net force on the sphere can be resolved into a 'lift' in the y-direction and a drag in the x-direction. The mean lift must vanish, but the root-mean-square lift is the same in all directions transverse to the mean flow, and may be evaluated by considering its value in the y-direction. Indeed, when $\varphi_n \neq 0$ the component of the lift $\mathscr{L}_n$, say, in the y-direction is obtained by first evaluating it for $\varphi_n = 0$ by taking $X_i = X_y \equiv y(1 + R^3/2|\boldsymbol{x}|^3)$ in (2.7), and then multiplying by $\cos\varphi_n$ to obtain

$$\mathscr{L}_n = \rho_o U_c \Gamma a \cos\varphi_n \mathscr{F}_n(t - t_n) \tag{2.10}$$

where

$$\mathscr{F}_n(t-t_n) = 0, \quad t < t_n$$
$$= \int_{-\xi_n(t)}^{\xi_n(t)} \cos\xi \left[1 + \frac{R^3(x_n^2(t) + 2ax_n(t)\cos\xi\sin\theta_n + a^2(1 - 3\cos^2\theta_n))}{2(x_n^2(t) + 2ax_n(t)\cos\xi\sin\theta_n + a^2)^{5/2}}\right] \mathrm{d}\xi,$$
$$t > t_n. \tag{2.11}$$

The drag $\mathscr{D}_n$ produced by the nth vortex ring is independent of φ_n and is calculated

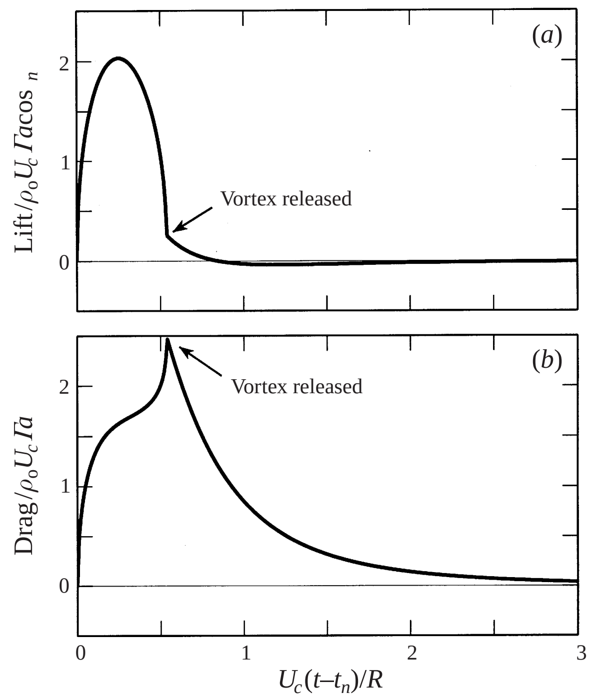

FIGURE 3. Variation of (*a*) the non-dimensional lift $\mathscr{L}_n/\rho_o U_c \Gamma a \cos\phi_n$, and (*b*) the drag $\mathscr{D}_n/\rho_o U_c \Gamma a$, during shedding from the sphere when $a = 0.7R$, $\theta_n = \pi/8$.

by setting $X_i = X_x$ in (2.5). This yields

$$\mathscr{D}_n = \rho_o U_c \Gamma a \mathscr{G}_n(t - t_n) \tag{2.12}$$

where

$$\begin{aligned} \mathscr{G}_n(t - t_n) &= 0, \quad t < t_n \\ &= \frac{3aR^3 \cos\theta_n}{2} \int_{-\xi_n(t)}^{\xi_n(t)} \frac{(x_n(t) + a\cos\xi \sin\theta_n)\,\mathrm{d}\xi}{(x_n^2(t) + 2ax_n(t)\cos\xi \sin\theta_n + a^2)^{5/2}}, \quad t > t_n. \end{aligned} \tag{2.13}$$

These integrals must be evaluated numerically. After release of the vortex from the sphere (so that $\xi_n(t) = \pi$) the magnitudes of the lift and drag decay very rapidly, and satisfy

$$\frac{\mathscr{L}_n}{\rho_o U_c \Gamma a} \sim \frac{\pi R^3 \cos\varphi_n}{U_c^3 (t - t_n)^3}, \quad \frac{\mathscr{D}_n}{\rho_o U_c \Gamma a} \sim \frac{3\pi a R^3 \cos\theta_n}{U_c^4 (t - t_n)^4} \quad \text{when } U_c(t - t_n) \gg R.$$

Figure 3 illustrates the dependence of the non-dimensional lift $\mathscr{L}_n/\rho_o U_c \Gamma a \cos\varphi_n$ and drag $\mathscr{D}_n/\rho_o U_c \Gamma a$ on time for the case in which $a = 0.7R$, $\theta_n = \pi/8$. The lift grows rapidly during the initial stages of shedding, attaining a maximum when roughly half the ring vortex has been formed; the subsequent release of vorticity of opposite sign reduces the net circulation around the sphere and causes the lift to decrease. After release the lift force slowly decays and is negligible when the ring has convected about a sphere diameter into the wake. On the other hand, the drag increases monotonically until the vortex is released, following which it decreases slowly and becomes negligible when the ring is about three diameters downstream. These results imply that the behaviour of the vortex in the distant wake (where it is not permissible to ignore the influences of turbulence diffusion and the misalignment of the vortex centres produced by self-induction) makes a very limited contribution to the unsteady surface force.

Equation (2.8) indicates that, in the initial stages of formation of the vortex, when $U_c(t-t_n) \ll R$,

$$\xi_n(t) \approx \left(\frac{2U_c(t-t_n)}{a}\right)^{1/2} \sqrt{\frac{\sqrt{R^2-a^2\cos^2\theta_n}}{a\sin\theta_n[\sqrt{R^2-a^2\cos^2\theta_n}-a\sin\theta_n]}},$$

which implies that

$$\frac{\mathscr{L}_n}{\rho_o U_c \Gamma a}, \quad \frac{\mathscr{D}_n}{\rho_o U_c \Gamma a} \sim \left(\frac{U_c(t-t_n)}{a}\right)^{1/2} \quad \text{when } U_c(t-t_n) \ll R. \tag{2.14}$$

In § 3 we shall make use of the following small-time approximation:

$$\frac{\mathscr{L}_n}{\rho_o U_c \Gamma a \cos\varphi_n} \approx 3\sqrt{\frac{2U_c(t-t_n)}{a}}\left[1-\left(\frac{a}{R}\right)^2\cos^2\theta_n\right] \times \left[\frac{\sqrt{R^2-a^2\cos^2\theta_n}}{\sin\theta_n[\sqrt{R^2-a^2\cos^2\theta_n}-a\sin\theta_n]}\right]^{1/2}, \tag{2.15}$$

which is valid for $U_c(t-t_n) \ll a\sin\theta_n$.

3. The lift and drag spectra

3.1. *The mean drag*

Periodic vortex shedding from the sphere can be simulated by assuming that the nth vortex ring begins to form at time

$$t_n = n\tau, \quad \tau \equiv \frac{1}{f_o}, \tag{3.1}$$

where the fundamental frequency $f_o \sim 0.2U/D$. The magnitude of the circulation Γ will be expressed in terms of the mean drag coefficient C_D of the sphere. To do this the representation (2.12) is used to write the mean drag in the form

$$\langle \mathscr{D}(t)\rangle = \rho_o U_c \Gamma a \sum_{n=-\infty}^{\infty} \langle \mathscr{G}_n(t-t_n)\rangle \tag{3.2}$$

where the angle brackets denote an average over an ensemble of realizations of the train of vortex rings. Introduce

$$\hat{\mathscr{G}}_n(\omega) = \frac{1}{2\pi}\int_0^{\infty} \mathscr{G}_n(t)\mathrm{e}^{\mathrm{i}\omega t}\,\mathrm{d}t, \tag{3.3}$$

the Fourier transform of $\mathscr{G}_n(t)$, and write

$$\langle \mathscr{D}(t)\rangle = \rho_o U_c \Gamma a \int_{-\infty}^{\infty} \sum_{n=-\infty}^{\infty} \langle \hat{\mathscr{G}}_n(\omega)\rangle \mathrm{e}^{-\mathrm{i}\omega(t-n\tau)}\,\mathrm{d}\omega. \tag{3.4}$$

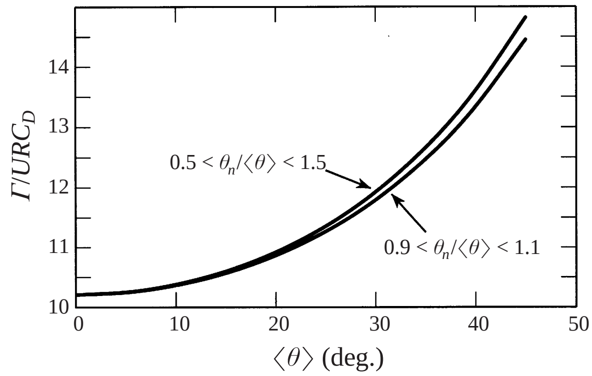

FIGURE 4. Dependence of the calculated circulation Γ on $\langle\theta\rangle \equiv \langle\theta_n\rangle$ for two cases in which θ_n is uniformly distributed about the mean.

The mean value $\langle\hat{\mathscr{G}}_n(\omega)\rangle$ is independent of n, and the Fourier expansion (Lighthill 1958)

$$\sum_{n=-\infty}^{\infty} \mathrm{e}^{\mathrm{i}\omega n\tau} = \frac{2\pi}{\tau} \sum_{m=-\infty}^{\infty} \delta\left(\omega - \frac{2\pi m}{\tau}\right), \tag{3.5}$$

therefore implies that

$$\langle\mathscr{D}(t)\rangle = \frac{2\pi\rho_o U_c \Gamma a}{\tau} \sum_{m=-\infty}^{\infty} \langle\hat{\mathscr{G}}_n(2\pi m f_o)\rangle \mathrm{e}^{-2\pi\mathrm{i}mf_o t}, \tag{3.6}$$

which shows how the ensemble-average drag varies with time at the fundamental shedding frequency f_o. The mean drag $\overline{\mathscr{D}}$ is obtained by averaging with respect to time, to obtain

$$\overline{\mathscr{D}} = \frac{2\pi\rho_o U_c \Gamma a}{\tau}\langle\hat{\mathscr{G}}_n(0)\rangle \equiv \frac{\rho_o U_c \Gamma a}{\tau} \int_0^\infty \langle\mathscr{G}_n(t)\rangle\,\mathrm{d}t. \tag{3.7}$$

However, $\overline{\mathscr{D}} = C_D \frac{1}{2}\rho_o U^2 A$ $(A = \pi R^2)$, so that equation (3.7) supplies

$$\frac{\Gamma}{UR} = \frac{\pi C_D}{2}\frac{R}{a}\frac{U}{U_c}\bigg/ \frac{1}{\tau}\int_0^\infty \langle\mathscr{G}_n(t)\rangle\,\mathrm{d}t. \tag{3.8}$$

The plots in figure 4 reveal that the circulation Γ is only weakly dependent on the extent of the range spanned by the vortex orientation angle θ_n. This figure shows the dependence of Γ/URC_D determined by (3.8) for the two cases in which $\theta_n/\langle\theta\rangle$ is assumed to be uniformly distributed respectively over the intervals (0.5, 1.5) and (0.9, 1.1) for a range of possible values of the mean orientation $\langle\theta_n\rangle \equiv \langle\theta\rangle$, and for the particular case in which $a = 0.7R$, $U_c = 0.7U$.

3.2. *The spectrum of the lift fluctuations*

The time-dependent lift experienced by the sphere in the y-direction is given by

$$\mathscr{L}(t) = \rho_o U_c \Gamma a \sum_{n=-\infty}^{\infty} \cos\varphi_n \mathscr{F}_n(t - t_n). \tag{3.9}$$

The mean lift vanishes because $\langle\cos\varphi_n\rangle = 0$, where the angle brackets denote an ensemble average. When successive vortices are statistically independent

$\langle \cos\varphi_n \cos\varphi_m \rangle = \frac{1}{2}\delta_{nm}$, and the mean-square lift becomes

$$\langle \mathscr{L}^2(t) \rangle = \frac{(\rho_o U_c \Gamma a)^2}{2} \sum_{n=-\infty}^{\infty} \langle \mathscr{F}_n^2(t - t_n) \rangle. \tag{3.10}$$

If $\hat{\mathscr{F}}_n(\omega)$ is the Fourier transform defined in terms of $\mathscr{F}_n(t)$ as in equation (3.3), we have

$$\langle \mathscr{L}^2(t) \rangle = \frac{(\rho_o U_c \Gamma a)^2}{2} \iint_{-\infty}^{\infty} \sum_{n=-\infty}^{\infty} \left\langle \hat{\mathscr{F}}_n(\omega) \hat{\mathscr{F}}_n^*(\omega') \right\rangle \mathrm{e}^{-\mathrm{i}(\omega-\omega')(t-n\tau)} \, \mathrm{d}\omega \mathrm{d}\omega', \tag{3.11}$$

where the asterisk denotes complex conjugate. As before, the ensemble average $\langle \hat{\mathscr{F}}_n(\omega) \hat{\mathscr{F}}_n^*(\omega') \rangle$ does not depend on n, so that the expansion (3.5) (with ω replaced by $\omega - \omega'$) leads to a time-averaged, mean-square lift

$$\overline{\mathscr{L}^2} = \frac{\pi(\rho_o U_c \Gamma a)^2}{\tau} \int_{-\infty}^{\infty} \langle |\hat{\mathscr{F}}_n(\omega)|^2 \rangle \, \mathrm{d}\omega. \tag{3.12}$$

The *one-sided* frequency spectrum of the lift $\Phi_L(\omega)$ satisfies

$$\overline{\mathscr{L}^2} = \int_0^{\infty} \Phi_L(\omega) \, \mathrm{d}\omega, \tag{3.13}$$

and we therefore have

$$\Phi_L(\omega) = (\rho_o U_c \Gamma a)^2 \frac{2\pi}{\tau} \langle |\hat{\mathscr{F}}_n(\omega)|^2 \rangle, \tag{3.14}$$

where the remaining average is to be taken over all possible orientations θ_n of a vortex ring with respect to the direction of the undisturbed mean stream.

Figure 5(a) illustrates predictions of the lift spectrum $10\log_{10}((U/D)\Phi_L(\omega)/(C_D \rho_o U^2 A)^2)$ (dB) plotted as a function of $\omega D/U$, where $A = \pi R^2$ is the frontal area of the sphere, for the two cases $\langle \theta \rangle = 10^\circ, 30^\circ$. Permissible vortex orientation angles θ_n are assumed to occupy the interval $\frac{1}{2} < \theta_n / \langle \theta \rangle < \frac{3}{2}$ with $a = 0.7R$, $U_c = 0.7U$. Average values have been computed using an ensemble of 100 vortex rings.

Both spectra are essentially the same for $\omega D/U > 10$, and decay like $1/\omega^3$ at high-frequencies. The high-frequency dependence is governed by the behaviour of the lift force during the initial stages of formation of a vortex ring. In fact, the ω^{-3}-dependence shown in figure 5(a) occurs because $\mathscr{L}_n \propto \sqrt{t - t_n}$ when $t - t_n \ll a \sin\theta_n / U_c$. By evaluating the Fourier transform $\hat{\mathscr{F}}_n(\omega)$ from the small-time approximation (2.15) we obtain (Lighthill 1958) the high-frequency representation

$$\Phi_L(\omega) \sim \frac{9U_c(\rho_o U_c \Gamma a)^2}{4\tau a \omega^3} \left\langle \left[1 - \left(\frac{a}{R}\right)^2 \cos^2\theta_n\right]^2 \left[\frac{\sqrt{R^2 - a^2\cos^2\theta_n}}{\sin\theta_n[\sqrt{R^2 - a^2\cos^2\theta_n} - a\sin\theta_n]}\right] \right\rangle, \tag{3.15}$$

which is applicable for $\omega D/U \gg D/a \sin\theta_n$. The prediction of this formula when $\langle \theta \rangle = 30^\circ$, using an ensemble of 100 vortex rings, is shown by the dotted straight line in figure 5(a).

Evidently the high-frequency behaviour of the spectrum does not depend on our assumption that the coherent eddies are modelled by vortex rings; in a more general view of the problem the length a in the approximation (3.15) would be interpreted as the *radius of curvature* of the initial thread of the large-scale vortex loops that are

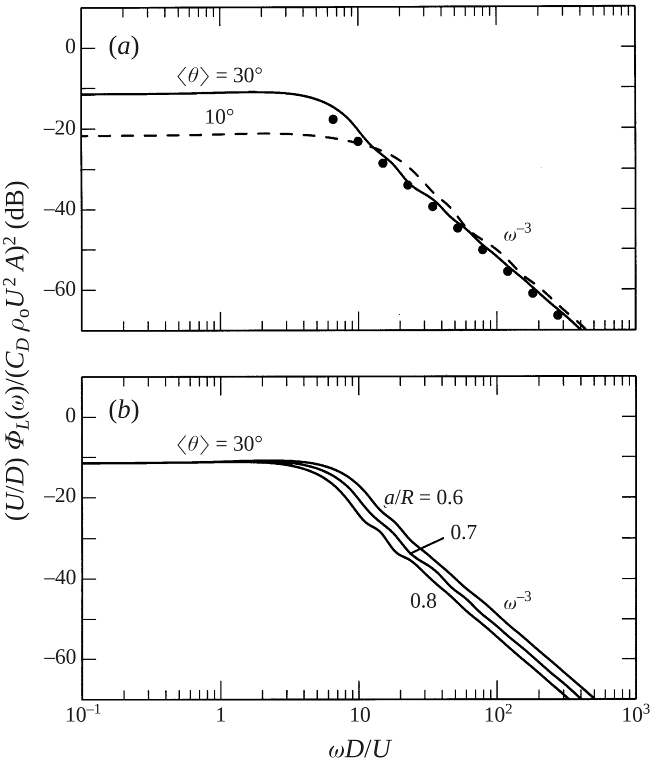

FIGURE 5. Non-dimensional lift spectrum $10\log_{10}((U/D)\Phi_L(\omega)/(C_D\rho_0 U^2 A)^2)$ (dB) for $U_c = 0.7U$ when averaging is performed over $(\frac{1}{2} < \theta_n/\langle\theta\rangle < \frac{3}{2})$: (*a*) $a/R = 0.7$ and $\langle\theta\rangle = 10°, 30°$, showing also the asymptotic approximation (3.15) (• • •) evaluated for $\langle\theta\rangle = 30°$; (*b*) $\langle\theta\rangle = 30°$ and $a/R = 0.6, 0.7, 0.8$.

periodically shed from the sphere. However, because it has been assumed that the vortex core diameter is infinitesimal, the asymptotic approximation must break down when $\omega D/U$ exceeds D/Δ, where Δ is a distance of the order of the initial vortex core diameter. For the experiments described in § 4, $D = 7.62$ cm, so that estimating Δ to be initially about 0.1 cm, the present theory would become inapplicable when fD/U exceeds about 10^2.

The dependence of these predictions on a/R, the ratio of the vortex ring radius to that of the sphere, is illustrated in figure 5(*b*), again for $\langle\theta\rangle = 30°$ and when the other parameters are unchanged. The simplicity of the analytical model, and the relative insensitivity of predictions to the diameter of the shed vortices, suggest that the nominal value $a/R = 0.7$ is probably representative of a high Reynolds number wake of reduced width immediately behind the sphere, and this value will be used in the discussion below in § 4.

3.3. *The spectrum of the drag fluctuations*

The frequency spectrum $\Phi_D(\omega)$ of the unsteady drag

$$\mathscr{D}'(t) = \mathscr{D}(t) - \langle\mathscr{D}\rangle,$$

is defined such that

$$\overline{\mathscr{D}'^2} = \int_0^\infty \Phi_D(\omega)\,\mathrm{d}\omega. \tag{3.16}$$

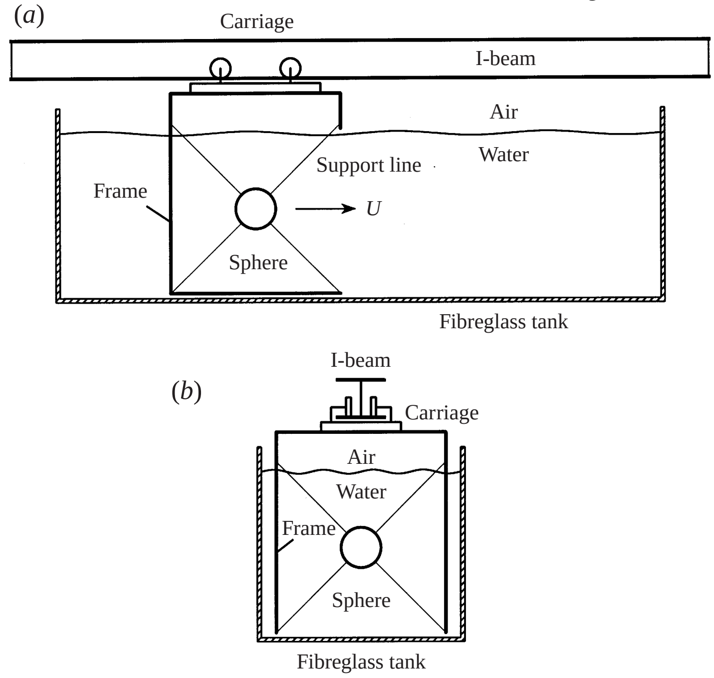

FIGURE 6. Schematic of the experimental arrangement: (*a*) the support lines of the sphere are configured for the measurement of the side-force (i.e. 'lift') fluctuations. (*b*) End-view of tank showing the configuration used for measuring the unsteady drag.

It is readily confirmed by following the procedure described above that

$$\Phi_D(\omega) = (\rho_o U_c \Gamma a)^2 \frac{4\pi}{\tau}\{\langle|\hat{\mathscr{G}}_n(\omega)|^2\rangle - |\langle\hat{\mathscr{G}}_n(\omega)\rangle|^2\}, \tag{3.17}$$

where the averages are with respect to the orientations θ_n of the vortex rings. The characteristics of the predicted spectrum are discussed in the next section.

4. Comparison with experiment

4.1. *Experimental apparatus*

Measurements of the unsteady lift and drag were made in the fibreglass towing tank of working length 9.2 m illustrated schematically in figure 6(*a*). The cross-section of the tank is $25.4 \times 25.4\,\mathrm{cm}^2$ and it is filled with water to a depth of 22 cm. A sphere of diameter 7.62 cm is supported in the water with its centre nominally on the longitudinal centreline (the x-axis) of the tank by four flexible, nylon lines each of which can withstand a tension of 89 N. The lines lie in a vertical meridian plane of the sphere, inclined at 45° to the vertical, so that neighbouring lines meet the surface of the sphere at an angular separation of 90°. They are secured to a vertical frame of aluminium rods bolted to the underside of a carriage suspended above the tank from wheels running smoothly along a horizontal, 10 m composite fibreglass I-beam mounted on an adjacent parallel concrete wall. The sphere can therefore execute small-amplitude translational vibrations (< 1 mm in amplitude) in the direction normal to the meridian plane. Figure 6(*a*) illustrates the configuration used for measuring the unsteady lift, where the meridian plane is parallel to the direction of motion of the carriage. The sphere translates parallel to the centreline of the tank at a constant mean speed when the carriage is towed along the track by means of a closed-loop horizontal cable connected to a computer-controlled drive motor situated at one end of the track. The apparatus is isolated from ambient vibrations in the measurement range of 10–60 Hz by mounting the tank on resilient floor supports and by inserting vibration dampers between the I-beam and the wall. A system involving an intermediate pulley and two flexible drive belts is used to minimize vibration transmission from the motor, which is itself placed in a foam-lined wooden box to minimize airborne noise from the motor. As a final precaution, all measurements were made when the laboratory automatic ventilation system was not in operation.

Two test spheres were constructed to facilitate separate measurements of the unsteady drag and lift. Each is made from a 14 : 3 mixture by volume of polystyrene micro-balloons and epoxy resin cast in a spherical mold. A Geospace Corporation GS20-DH7 geophone is encased at the centre of a sphere during fabrication. The signal cable from the geophone leaves the sphere at the rearward stagnation point and is connected to a Hewlett Packard 3567A spectrum analyzer via a preamplifier. The voltage output from the geophone is proportional to the velocity of the sphere, and the geophone is orientated within the sphere with its axis normal to the meridian plane of support. The output at different frequencies, when multiplied by frequency, is proportional to acceleration which, in turn, is related to the component of the force exerted on the sphere in the direction normal to the meridian plane by calibrating its response against that of a standard accelerometer attached to the sphere when the sphere is set into forced motion by a Wilcoxon Research F3 electromagnetic shaker. The force is determined from Newton's second law, including a correction to allow for the added mass (one half of the mass of water displaced by the sphere). The unsteady drag is measured by orientating the meridian plane of the aluminium support frame perpendicular to the axis of the tank, as illustrated in figure 6(*b*).

To inhibit the formation of surface air bubbles each sphere was immersed for 30 min in a solution of Kodak Photo-Flo 200 wetting agent before each calibration and measurement. The tests were performed by towing at one of four different speeds of 10, 15, 20 and 25 cm s^{-1}, corresponding to Reynolds numbers ranging from about 7000 to 17 000, and storing electronically the output from the geophone.

Similar towing tank measurements of the lift have been reported by Lauchle & Jones (1998) for the case in which the sphere mimics a submerged hydrophone, suspended as in practical applications. It was free to move with the unsteadiness created by the flow over its surface, and the force was determined using a geophone of the kind described above. However, the quality of force measurements is crucially dependent on the mode of suspension of the sphere. Lauchle & Jones (1998) used a three-point suspension, but the suspension lines did not lie in the same plane, and oscillations of the sphere were therefore possible in directions other than that of the lift (the z-direction in figure 2). This permitted the geophone to respond to the unsteady drag, to the orthogonal (*vertical*) component of lift, and to moments created by the flow, causing their measurements to underestimate the unsteady side force. Furthermore, the three-point suspension cannot be used to measure the unsteady drag, because the steady drag rotates the sphere backward from its towing orientation, thereby causing the geophone to become misaligned with the streamwise (x-) direction. These problems do not arise with the present four-point suspension system.

However, there are two important limitations that require comment. First, the towing speed could not exceed about 25 cm s^{-1}. At this speed in water at 20 °C, the Reynolds number of a suspension line based on its diameter (0.033 cm) is about 82. The wake behind a line is therefore laminar, and should have a negligible influence on the unsteady force on the sphere. But, the aluminium support rods are 0.4 cm in diameter, with Reynolds number ~ 988 at $25\,\mathrm{cm\,s^{-1}}$; their wakes are therefore unstable and within the range of turbulent vortex cores, and could influence the force measurement. Therefore, higher towing speeds were not considered.

Second, measurements were not made for frequencies greater than 60 Hz. Several spurious peaks in the power spectra were observed at higher frequencies. These peaks do not change with towing speed and can therefore be attributed to structural resonances of the suspension system. Increasing the diameter (and the stiffness) of the support rods will reduce these vibrations, but will also increase the Reynolds number into the range where vortex shedding contaminates the force measurements.

The practical effect of these precautions is to eliminate 'gross', uncontrolled motions of the sphere, while at the same time permitting the sphere to vibrate at very small amplitude in either the lift or drag direction without degrading the sensitivity of the geophone. The measured displacement of the sphere at frequencies exceeding 10 Hz is so small that it cannot be seen with the naked eye. For a freely falling or tethered sphere, on the other hand, large displacements from a uniform trajectory are observed at frequencies comparable to the shedding frequency.

Further details of the construction of the apparatus and the experimental procedure are given by Wang (1999).

4.2. *Results*

Spectral data were recorded during several runs at each towing speed, and the final spectral level at each frequency was obtained by averaging over an ensemble of 100 time series. This is large enough to ensure that the random error at each velocity does not exceed about ± 0.4 dB. The corresponding errors when measurements at the four different towing speeds are combined and plotted against Strouhal number were about ± 2 and ± 3 dB respectively for the lift and drag. In all cases the background noise for a stationary carriage was about 30 dB smaller than the measurements.

The solid circles in figures 7(*a*) and 7(*b*) respectively represent average measured values of the lift and drag spectra $10\log_{10}((U/D)G_L(f)/(\rho_o U^2 A)^2)$, $10\log_{10}((U/D)G_D(f)/(\rho_o U^2 A)^2)$, plotted against the Strouhal number fD/U, where $f = \omega/2\pi$ is the frequency in Hz, and

$$G_L(f) = 2\pi\Phi_L(\omega), \quad G_D(f) = 2\pi\Phi_D(\omega). \tag{4.1}$$

This normalization ensures that $\overline{\mathscr{L}^2} = \int_0^\infty G_L(f)\,\mathrm{d}f$ and $\overline{\mathscr{D}'^2} = \int_0^\infty G_D(f)\,\mathrm{d}f$. The vertical error bars in these figures indicate the spread of the experimental results for the four different towing speeds, i.e. they represent a possible residual influence of Reynolds number on the lift and drag over the range $Re = 7000$ to 17 000, or possibly a Reynolds number effect associated with unsteady forces on the frame and support lines.

Also shown in figure 7(*a*) are the low-frequency lift data from the experiments conducted in air by Willmarth & Enlow (1969). These were performed at the very much higher (supercritical) Reynolds numbers of 4.84×10^5, 8.26×10^5, 16.46×10^5, 16.67×10^5, and the open squares in the figure represent results for each Strouhal number averaged over these Reynolds numbers, the error bar again representing the data spread.

The solid and broken curves in figures 7(*a*) and 7(*b*) are the corresponding predictions of $G_L(f), G_D(f)$ determined by equations (3.14), (3.17) respectively for $\langle\theta\rangle = 30^\circ, 10^\circ$. As before the vortex orientation angles θ_n are assumed to occur within the interval $\frac{1}{2} < \theta_n/\langle\theta\rangle < \frac{3}{2}$ with $a = 0.7R, U_c = 0.7U$, and we have taken $C_D = 0.4$. This value for the drag coefficient is appropriate over the whole of the subcritical region where $Re > 10^3$ (Schlichting 1979). Average values have been computed using an ensemble of 100 vortex rings.

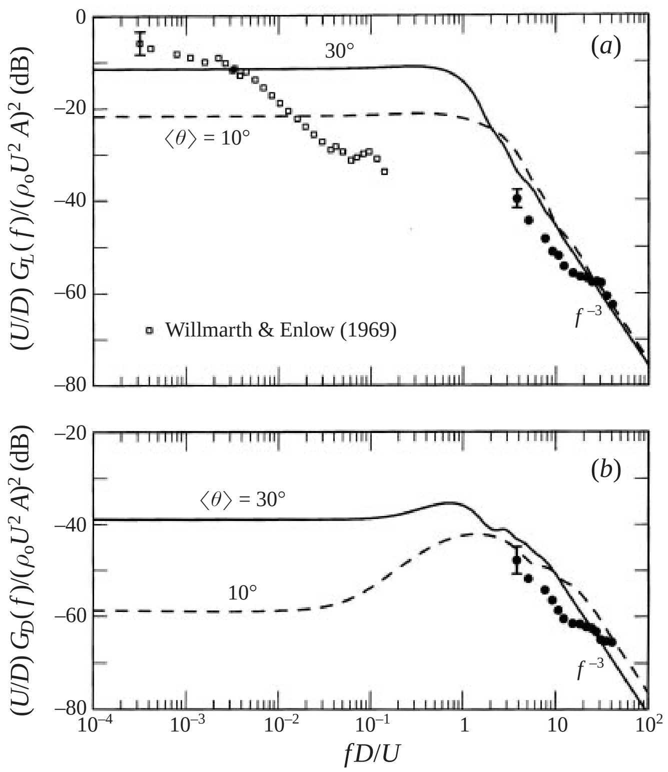

FIGURE 7. Measured and predicted (*a*) lift spectrum $10\log_{10}((U/D)G_L(f)/(\rho_o U^2 A)^2)$ (dB) and (*b*) drag spectrum $10\log_{10}((U/D)G_D(f)/(\rho_o U^2 A)^2)$ (dB): • • •, averaged measured values for $Re = 6680$, 10 020, 13 360, 16 700. Predictions are shown for the two cases $\langle\theta\rangle = 10°, 30°$ when averaging is performed over $(\frac{1}{2} < \theta_n/\langle\theta\rangle < \frac{3}{2})$ and $a = 0.7R$, $U_c = 0.7U$, $C_D = 0.4$. Also shown in (*a*) is the low-frequency data of Willmarth & Enlow (1969).

At high Strouhal numbers both sets of theoretical curves decrease like $1/f^3$, independently of the value of $\langle\theta\rangle$, and this is close to the trend of the experimental data. The remarkable accord in the absolute levels between theory and experiment indicates that the proposed model, according to which the unsteady surface forces are determined by coherent vortex shedding, is correct in principle if not in detail, inasmuch as the high-frequency behaviour of the spectra is determined by the initial stages in the shedding of a vortex structure. The wind tunnel experiments of Willmarth & Enlow (1969) were performed in air at speeds between 50 and 150 ft s^{-1} (15.25 and 45.75 m s^{-1}). In these experiments, when $fD/U < 10^{-1}$ the length scale of disturbances in the wake of the sphere $\sim U/f > 10D \geqslant 6$ m, which is four times the smallest cross-sectional dimension of the wind tunnel and comparable to the length of the working section of the tunnel. At very low frequencies a coherent vortex structure in the wake will therefore extend beyond the end of the working section of the wind tunnel. In these circumstances the free field calculations of §§2, 3 cannot represent correctly the characteristics of the measured lift fluctuations, and this presumably accounts for the ambiguous correspondence in figure 7(*a*) between theory and experiment at low Strouhal numbers.

If one plots a swath that straddles the experimental data by the error bars indicated on figure 7, the spectral predictions are within 2–4 dB of that swath. The spectral swaths maintain the same slope as the theory but are shifted in magnitude by about

4 dB from the theoretical levels at Strouhal numbers below 10. There is a 'step' in both sets of data between Strouhal numbers of about 10 and 45. In this range most of the data that are shown were obtained at the lowest towing speeds of 10 and 15 cm s^{-1} ($Re = 6680$–$10\,020$). Measurements were not made at lower speeds because the signal-to-background noise ratio was then unacceptable: for Re between 3000 and about 6000 there is a transition of the vortex rings from a laminar to a turbulent regime (Sakamoto & Haniu 1990), and the signal is not strong enough to be measured reliably in this transition region (or at lower Reynolds numbers). It is suspected that the measurement uncertainties quoted above, of ± 2 and ± 3 dB respectively for the lift and drag, may be slightly larger for $16 < fD/U < 45$, but there was no way of establishing this tolerance to any better accuracy. Consequently there is a small discrepancy between the predicted and measured spectral slopes at higher Strouhal numbers.

It is particular noteworthy that for both theory and experiment the unsteady drag fluctuations are 5 dB or more smaller than the lift fluctuations at high frequencies. This is consistent with the numerical results of Zierke (1997).

5. Conclusion

A non-spinning sphere in high Reynolds number, nominally steady, incompressible flow experiences unsteady lift and drag. Correlation measurements have linked the net force on the sphere to fluctuations in the bound vorticity in the meridian plane normal to the force, and it has long been conjectured that these fluctuations in bound vorticity arise from the shedding of large-scale coherent structures into the wake, even at supercritical Reynolds numbers. The model of coherent vortex shedding proposed in this paper considers the wake to consist of a succession of randomly orientated vortex rings, interconnected by pairs of oppositely rotating vortices, and shed at quasi-periodic intervals at a Strouhal number ~ 0.19. At high Reynolds number coherent wake structures of this kind must be rapidly dissipated by turbulence diffusion. However, the dominant surface force is determined by the nascent vortex ring and, moreover, the force spectrum at Strouhal numbers $fD/U > 1$ is governed by the initial stages of formation of the ring, and is therefore effectively independent of the shape of the fully formed vortex. Predictions of the lift and drag spectra based on this model are in close agreement with new towing tank measurements at intermediate Reynolds number for $fD/U > 1$. At smaller Strouhal numbers the predictions are more strongly influenced by hypotheses regarding the orientation and statistics of vortex rings, but still exhibit an acceptable level of agreement with the earlier lift measurements of Willmarth & Enlow (1969).

The research reported in this paper was supported by grants from the Office of Naval Research, Code 321 SS (Mr Scott Littlefield), Code 333 (Dr Kam Ng), and from the Naval Air Warfare Center, Aircraft Division (Dr James McEachern). M. S. H. acknowledges the support provided by the Applied Research Laboratory at Penn State University during a sabbatical appointment.

REFERENCES

Achenbach, E. 1972 Experiments on the flow past spheres at very high Reynolds numbers. *J. Fluid Mech.* **54**, 565–575.

Achenbach, E. 1974 Vortex shedding from spheres. *J. Fluid Mech.* **62**, 209–221.

Barton, N. G. 1982 On the swing of a cricket ball in flight. *Proc. R. Soc. Lond.* A **379**, 109–131.

Chomaz, J. M., Bonneton, P. & Hopfinger, E. J. 1993 The structure of the near wake of a sphere moving horizontally in a stratified fluid. *J. Fluid Mech.* **254**, 1–21.

Finger, R. A., Abbagnaro, L. A. & Bauer, B. B. 1979 Measurement of low-velocity flow noise on pressure and pressure gradient hydrophones. *J. Acoust. Soc. Am.* **65**, 1407–1412.

Gabrielson, T. B., Gardner, D. L. & Garrett, S. L. 1995 A simple neutrally buoyant sensor for direct measurement of particle velocity and intensity in water. *J. Acoust. Soc. Am.* **97**, 2227–2237.

Goldstein, S. (Ed.) 1965 *Modern Developments in Fluid Dynamics*, Volume 2. Dover.

Howe, M. S. 1989 On unsteady surface forces, and sound produced by the normal chopping of a rectilinear vortex. *J. Fluid Mech.* **206**, 131–153.

Howe, M. S. 1998 *Acoustics of Fluid-Structure Interactions*. Cambridge University Press.

Hunt, J. C. R., Kawai, H., Ramsey, S. R., Pedrizetti, G. & Perkins, R. L. 1990 A review of velocity and pressure fluctuations in turbulent flows around bluff bodies. *J. Wind Engng Indust. Aero.* **35**, 49–85.

Johnson, T. A. & Patel, V. C. 1999 Flow past a sphere up to a Reynolds number of 300. *J. Fluid Mech.* **378**, 19–70.

Keller, B. D. 1977 Gradient hydrophone flow noise. *J. Acoust. Soc. Am.* **62**, 205–208.

Kim, H. J. & Durbin, P. A. 1988 Observations on the frequencies in a sphere wake and of drag increase by acoustic excitation. *Phys. Fluids* **31**, 3260–3265.

Lauchle, G. C. & Jones, A. R. 1998 Unsteady lift force on a towed sphere. *J. Fluids Struct.* **12**, 949–958.

Leslie, C. B., Kendall, J. M. & Jones, J. L. 1956 Hydrophone for measuring particle velocity. *J. Acoust. Soc. Am.* **28**, 711–715.

Lighthill, M. J. 1958 *An Introduction to Fourier Analysis and Generalised Functions*. Cambridge University Press.

McEachern, J. F. & Lauchle, G. C. 1995 Flow-induced noise on a bluff body. *J. Acoust. Soc. Am.* **97**, 947–953.

Mittal, R. 1999 Planar symmetry in the unsteady wake of a sphere. *AIAA J.* **37**, 388–390.

Parkinson, G. 1989 Phenomena and modeling of flow-induced vibrations of bluff bodies. *Prog. Aerospace Sci.* **26**, 169–224.

Phillips, O. M. 1956 The intensity of Aeolian tones. *J. Fluid Mech.* **1**, 607–624.

Rayleigh & Lord 1877 On the irregular flight of a tennis-ball. *Mess. Math.* **7**, 14–16 (also *Scientific Papers* **1** (53), 344–346; Dover 1964).

Sakamoto, H. & Haniu, H. 1990 A study on vortex shedding from spheres in uniform flow. *Trans. ASME: J. Fluids Engng* **112**, 386–392.

Schlichting, H. 1979 *Boundary Layer Theory*, 7th Edn. McGraw-Hill.

Scoggins, J. R. 1967 Sphere behavior and the measurement of wind profiles. *NASA Tech. Note* D-3994.

Taneda, S. 1956 Experimental investigation of the wake behind a sphere at low Reynolds numbers. *J. Phys. Soc. Japan* **11**, 1104–1108.

Taneda, S. 1978 Visual observations of the flow past a sphere at Reynolds numbers between 10^4 and 10^6. *J. Fluid Mech.* **85**, 187–192.

Tomboulides, A. G. & Orszag, S. A. 2000 Numerical investigation of transitional and weak turbulent flow past a sphere. *J. Fluid Mech.* **416**, 45–74.

Tomboulides, A. G., Orszag, S. A. & Karniadakis, G. E. 1993 Direct and large-eddy simulation of axisymmetric wakes. *AIAA Paper* 93-0546.

Wang, J. 1999 Hydrodynamic lift and drag fluctuations on a sphere. Doctoral thesis, The Pennsylvania State University.

West, G. S. & Apelt, C. S. 1993 Measurements of fluctuating pressures and forces on a circular cylinder in the Reynolds number range 10^4 to 2.5×10^5. *J. Fluids Struct.* **7**, 227–244.

Williamson, C. H. K. & Govardhan, R. 1997 Dynamics and forcing of a tethered sphere in a fluid flow. *J. Fluids Struct.* **11**, 293–305.

Willmarth, W. W. & Enlow, R. L. 1969 Aerodynamic lift and moment fluctuations of a sphere. *J. Fluid Mech.* **36**, 417–432.

Zierke, W. C. (Ed.) 1997 A physics-based means of computing the flow around a maneuvering underwater vehicle. *The Pennsylvania State University Applied Research Laboratory Tech. Rep.* TR 97-002.